An algorithm for identifying the initiation of synoptic-scale Rossby waves on PV waveguides

Matthias Röthlisberger[a]*, Olivia Martius[a,b], Heini Wernli[c]

[a]*Oeschger Centre for Climate Change Research and Institute of Geography, University of Bern, Bern, Switzerland*

[b]*Mobiliar Lab for Natural Risks, University of Bern, Bern, Switzerland*

[c]*Institute for Atmospheric and Climate Science, ETH Zurich, Zurich, Switzerland*

*Correspondence to: Matthias Röthlisberger, Institute of Geography, University of Bern, Hallerstrasse 12, 3012 Bern Switzerland.

E-mail: matthias.roethlisberger@giub.unibe.ch

In this study a novel method is presented that automatically identifies the initiation of synoptic-scale Rossby waves (RWIs) on potential vorticity (PV) waveguides. RWIs are identified based on geometry changes of the 2 Potential Vorticity Units (PVU) contour on two isentropic levels (320 and 340 K). The 2 PVU contours are hereby regarded as proxies for the position and shape of the extratropical and subtropical waveguide respectively. A RWI is recorded in a zonally aligned (i.e. wave-free) longitudinal contour segment if it becomes wavy over time and, additionally, the respective 2 PVU contour is wave-free upstream of the segment. To illustrate the potential of the method, three example RWIs are presented which reveal distinct initiation mechanisms. In the first RWI, a large convective system triggers a Rossby wave on the extratropical waveguide. In the second case, the two waveguides are vertically co-aligned and a meso-scale lower-stratospheric high-PV anomaly leads to the initiation of a Rossby wave on both waveguides. The third case illustrates the interaction between the two waveguides. A breaking wave on the extratropical waveguide steers a lower-stratospheric high-PV anomaly into close proximity with the undisturbed subtropical waveguide and induces a wave on the latter. The method is applied to ERA-Interim data from 1979 to 2014 in order to produce a feature-based climatology of RWIs on the two waveguides in the Northern Hemisphere during winter. The three main regions where RWIs occur are the Northwestern Pacific, North America and the North Atlantic, as well as North Africa and the Middle East.

This article has been accepted for publication and undergone full peer review but has not been through the copyediting, typesetting, pagination and proofreading process, which may lead to differences between this version and the Version of Record. Please cite this article as doi: 10.1002/smj.2690

Key Words: Rossby waves; Rossby wave initiation; identification algorithm; waveguide dynamics; feature-based; climatology; potential vorticity

Received . . .

1. Introduction

Synoptic-scale Rossby waves are ubiquitous features of the extratropical atmospheric flow and together with jets and vortices they form the building blocks of synoptic dynamics. On upper-level weather charts they are visible as synoptic-scale meridional undulations in the geopotential or the isentropic potential vorticity (PV) field, as well as in the potential temperature field on PV surfaces. In storm track regions the upper-level Rossby waves interact with the surface baroclinicity and create cyclones and anticyclones (e.g., Hoskins *et al.* 1985). After a phase of non-linear amplification, Rossby waves often break in the exit regions of the storm tracks (Thorncroft *et al.* 1993), where they can act as precursors to high impact weather (Massacand *et al.* 2001; Martius *et al.* 2008a). For example, strong surface cyclones (Wirth and Eichhorn 2014), heavy precipitation (Martius *et al.* 2008a) as well as temperature extremes (Screen and Simmonds 2014; Palmer 2014) can be preceded by high-amplitude Rossby waves and there is currently a vivid discussion of the linkage between changing Rossby wave characteristics and extreme events (e.g., Screen and Simmonds 2014; Coumou *et al.* 2014; Hoskins and Woollings 2015).

Furthermore, for weather forecasting, synoptic-scale Rossby waves are of eminent importance. Forecast errors closely follow the time evolution of individual Rossby wave crests (Davies and Didone 2013) and error patterns propagate with velocities close to the group velocity of Rossby waves (Langland *et al.* 2002; Hakim 2005). Thus, erroneous forecasts of the formation or propagation of Rossby waves lead to serious downstream errors (Rodwell *et al.* 2013). From a predictability point of view, this highlights the importance of a detailed process understanding already of the early stages in the life cycle of synoptic-scale Rossby waves.

Rossby waves propagate along two types of waveguides: (i) along the gradient of planetary vorticity, which acts as a waveguide for planetary waves that are triggered in the tropics and propagate into the extratropics (e.g., Hoskins and Karoly 1981) and (ii) along zonally extended and meridionally tight bands of strong PV gradients that are co-located with the extratropical and subtropical jet streams, which act as waveguides in the subtropics and extratropics (Hoskins and Ambrizzi 1993; Schwierz *et al.* 2004; Martius *et al.* 2010). While propagating along waveguides, Rossby wave dispersion leads to downstream development. Following Chang (1993) and Hakim (2003), downstream development is understood as the successive formation of troughs and ridges downstream of an existing trough or ridge on the same waveguide. Such a succession of troughs and ridges is frequently referred to as a Rossby wave train or Rossby wave packet (Lee and Held 1993; Glatt and Wirth 2014; Souders *et al.* 2014a).

Investigating relevant properties of Rossby wave packets such as their group velocity, their intensity, preferred pathways and preferred formation and lysis locations has been the subject of several studies (e.g. Chang and Yu 1999; Glatt and Wirth 2014; Souders *et al.* 2014a). In the Northern Hemisphere, Rossby wave packets typically form in the entrance regions of the storm tracks (Souders *et al.* 2014a) and persist up to several weeks (Glatt and Wirth 2014). Their number and intensity exhibits significant seasonal variability, with more numerous and more intense Rossby wave packets forming during winter (Glatt and Wirth 2014). In this study we focus specifically on regions where the first wave crest of a Rossby wave packet forms and investigate the mechanisms leading to the initiation of Rossby waves on PV waveguides.

Several initiation mechanisms for synoptic-scale Rossby waves have been proposed. From a PV perspective, they all illustrate ways how meso- to synoptic-scale PV anomalies can be brought to or generated near a wave-free PV waveguide. Davies and Didone (2013) separated these disturbances into two categories: (i) upper-tropospheric low-PV anomalies and (ii) lower-stratospheric high-PV anomalies.

Upper-tropospheric low-PV anomalies in the vicinity of a wave-free waveguide may result from weather systems associated with strong diabatic heating, including tropical cyclones (TCs) recurving from the tropics (Jones *et al.* 2003; Riemer *et al.* 2008; Grams *et al.* 2011; Archambault *et al.* 2013), warm-conveyor-belts in extratropical cyclones (Madonna *et al.* 2014) and conceivably large convective systems (Rodwell *et al.* 2013). In all of these systems, strong diabatic processes lead to upper-level low-PV anomalies in the outflow regions (Wernli and Davies 1997).

Lower-stratospheric high-PV anomalies approaching a wave-free waveguide from the poleward side are able to perturb the waveguide and trigger waves (e.g. Schwierz *et al.* 2004; Kew *et al.* 2010; Davies and Didone 2013). One form of such stratospheric PV anomalies are meso to synoptic-scale lower-stratospheric high-PV anomalies (Kew *et al.* (2010), also called tropopause polar vortices (Cavallo and Hakim 2009) and coherent tropopause disturbances (e.g. Pyle *et al.* 2004)), which are ubiquitous during winter and occur preferentially over the Canadian Arctic and Greenland (Cavallo and Hakim 2009; Kew *et al.* 2010). A second form of a stratospheric PV anomaly is a meridionally amplifying and breaking Rossby wave on the extratropical waveguide which brings high-PV air towards the subtropical waveguide and leads to the initiation of a wave on the latter (Martius *et al.* 2010). A requirement for this initiation mechanism is the co-occurrence of two waveguides at the same longitude. In winter, such a double jet configuration is frequent over Europe and North Africa (Koch *et al.* 2006; Martius *et al.* 2010). Additionally, wave breaking is frequent on the extratropical jet over Europe in this season (Martius *et al.* 2008b) and the subtropical jet over Africa is often zonally aligned (Koch *et al.* 2006). Thus, waveguide interaction might lead to RWIs occurring on the subtropical jet over North Africa and the Middle East.

After their formation, initial disturbances are often amplified by means of baroclinic instability, i.e. the reinforcing interaction between upper-level PV and surface potential temperature anomalies (Hoskins *et al.* 1985; Heifetz *et al.* 2004). Because baroclinic development requires pre-existing disturbances, we consider baroclinic instability as fundamentally important for wave amplification but not as a initiation mechanism per se.

The diversity of the potentially relevant dynamical initiation mechanisms, as well as its relevance for forecasting makes the initiation of synoptic-scale Rossby waves an attractive research topic. However, in recent studies on the dynamics and structure of synoptic-scale Rossby waves, the first stage of their life cycle has received little attention. Moreover, none of the recently developed methods to detect and track Rossby wave packets (e.g. Glatt and Wirth 2014; Souders *et al.* 2014b) was specifically designed to identify the exact initiation time and location of the first wave crest of a forming wave packet. In this study we address this research gap in the following three steps:

1. Develop an objective identification algorithm for RWIs.
2. Analyse individual RWIs as a proof of concept and in order to illustrate the potential of the identification algorithm.
3. Compile a Northern Hemisphere winter climatology of RWIs on the extratropical and subtropical waveguides.

The remainder of this paper is organized as follows: In Section 2.1 we introduce the data used in this study. Then, in Sections 2.2 and 2.3 the concept and the implementation of the identification algorithm are presented. Thereafter, as a first application of the identification algorithm, we discuss selected RWIs and the responsible initiation mechanisms in Section 3.1. Then, in Section 3.2, we present the climatology of Northern Hemisphere RWIs for winter from December 1979 to February 2014. Finally, Section 4 summarizes the main findings.

2. Data and Methods

2.1. Data

This study uses ERA-Interim data (Dee *et al.* 2011) for winters (December to February, DJF) in 1979/80-2013/14. ERA-Interim fields are available at 60 vertical levels (hybrid σ-p-levels, from the surface to 0.1 hPa) and at 6-hourly temporal resolution. For this study,

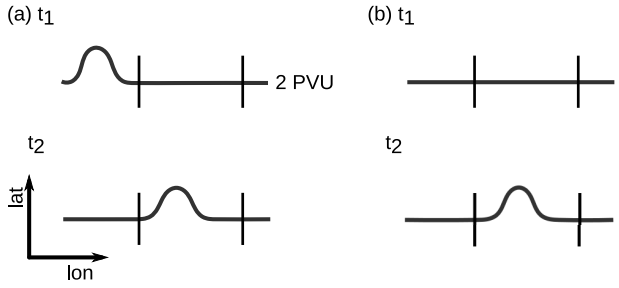

Figure 1. Schematic of the two possibilities for increasing waviness in a originally wave-free contour segment between times t_1 and t_2. Black lines indicates the 2 PVU contour on an isentrope. Vertical lines depict wave free contour segments at t_1. (a) waviness increases due to an upstream wave propagating into the contour segment, (b) waviness increases without an upstream wave, hence due to an in-situ process.

the data has been interpolated from a T255 spectral resolution to a regular grid with $1^\circ \times 1^\circ$ horizontal resolution and to isentropes and pressure levels. Additionally, in Section 3.1.1 infrared (IR) data from the GridSat-B1 dataset (Knapp *et al.* 2011) is used.

2.2. Concept of the identification algorithm

As synoptic-scale Rossby waves propagate along upper-level waveguides, i.e. areas of strong isentropic PV gradients along the dynamical tropopause, the geometry of these PV waveguides is indicative for the presence or absence of synoptic-scale Rossby waves. We use the 2 PVU contours on middle-world isentropes as proxy for the position and shape of the waveguides (1 PVU $\equiv 10^{-6}$ m^2 s^{-1} K kg^{-1}). Zonally aligned contour segments (extending over a distance similar or longer than the wave-length of a synoptic-scale Rossby wave) indicate an undisturbed waveguide while contour segments with large meridional undulations, i.e. areas with high waviness, indicate the presence of Rossby waves. Waviness increasing over time in a formerly wave-free contour segment can have two reasons. Either, the waviness increases due to a Rossby wave propagating into the segment from upstream (schematically illustrated in Figure 1(a)) or the waviness increases without an upstream wave and hence must be initiated in situ (Figure 1(b)). We are interested in the second case and further refer to such cases as initiation of a synoptic-scale Rossby wave (RWI). Following this concept, RWIs can be identified wherever a wave-free contour segment becomes wavy without an upstream wave being present. To implement this concept into an objective identification algorithm, a quantitative measure of the waviness of 2 PVU contour segments is needed. In addition, criteria are required to distinguish the two mechanisms for increasing waviness.

2.3. Implementation

Segment identification

We follow the ideas outlined above and first extract, at every time step, the 2 PVU contour on 320 K and 340 K. During the months analysed here (DJF) and in the climatological mean the extratropical and the subtropical waveguides are co-located with the dynamical tropopause on these two isentropic levels (Martius *et al.* 2010). Similarly to Wernli and Sprenger (2007), the 2 PVU contour encircling the pole is identified as a polygon of points, with longitude λ and latitude ϕ, with a fixed distance of 30 km between consecutive points. The waviness of a 2 PVU contour is then analysed for contour segments with 60 $^\circ$ longitude extension. At each time step t, 120 contour segments ($j = 1...120$) are identified, one starting every 3 $^\circ$ longitude. Each segment j consists of N_j points $[(\lambda_i, \phi_i), i = 1...N_j]$ and starts at longitude $(j-1) \cdot \Delta\lambda$ with $\Delta\lambda = 3^\circ$ and ends at longitude $(j-1) \cdot \Delta\lambda + 60^\circ$. Moving along the contour in the downstream direction, the starting point of each segment is identified as the intersection of this contour with the western-most meridian of the longitudinal segment. This contour is then followed in the downstream direction until it intersects the eastern-most meridian of the longitudinal segment.

Figure 2 illustrates the selection procedure of the contour segments. The green contour segment (segment no. 1) starts at the first crossing of the 2 PVU contour and the 0 $^\circ$ meridian when following the contour in the anticlockwise (downstream) direction and ends

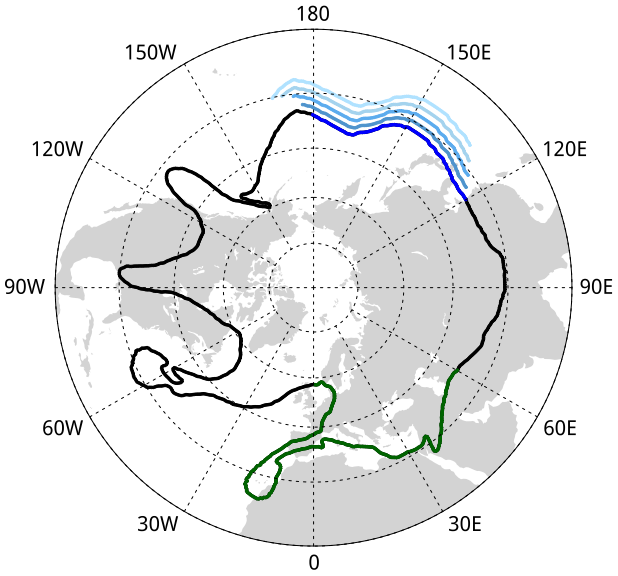

Figure 2. 2 PVU contour on 320 K in the Northern Hemisphere at 0600 UTC 27 February 2000 (solid black line). Segments no. 1, and nos. 41-45 are indicated in green and blue to light blue, respectively. Segments nos. 42-45 are shifted to the south for visibility reasons.

at 60 °E. Segments nos. 41–45 (blue to light blue) illustrate the overlapping of the 120 contour segments. The choice of the segment length depends on the wavelength and the phase velocity of the waves of interest. Ideally, the segment length is chosen such that newly forming wave crests are located entirely within one segment during their entire formation. For synoptic-scale waves with wavenumbers 5–10 and phase velocities of up to 15 ° longitude per day (Hovmöller 1949; Chang and Yu 1999) we found a segment length of 60 ° to be most appropriate. Different segment lengths were tested and a more detailed discussion on our choice of 60 ° is presented in the Supporting Information.

Waviness measure d

To measure the waviness of a contour segment a waviness measure d is defined as the sum of absolute values of latitude differences between consecutive points of the contour segment. For each segment j at a time t, the waviness d_j^t is thus calculated as

$$d_j^t = \sum_{i=1}^{N_j-1} |\phi_{i+1} - \phi_i| \tag{1}$$

where as before ϕ_i is the latitude of the contour at point i and N_j is the number of contour points of the segment j. Figure 3 schematically illustrates the calculation of d for a contour segment consisting of 9 points. The d-value of this segment is obtained by adding the lengths of the bars, which indicate the latitude difference between consecutive points. Note that d is different from the waviness measure introduced by Riemer and Jones (2014).

The waviness measure d has the following advantageous properties. For a perfectly zonal contour segment d is zero and for a segment covering a growing wave crest d increases linearly with the amplitude of the wave crest, as long as the wave crest is located entirely within the segment. Further, d is independent of the number of points chosen along the contour segment, as long as the main contour structures along the segment are resolved. Moreover, d is independent of the latitude at which a segment is located. This is an important property of d as it allows for directly comparing the waviness of segments located at different latitudes.

d-Hovmöller diagrams

Calculating d for all 120 segments over a number of time steps T (hereafter referred to as $d_j^t, j = 1...120, t = 1...T$) results in a longitude-time information of the waviness of the 2 PVU contour on the considered isentrope, which can be depicted succinctly in

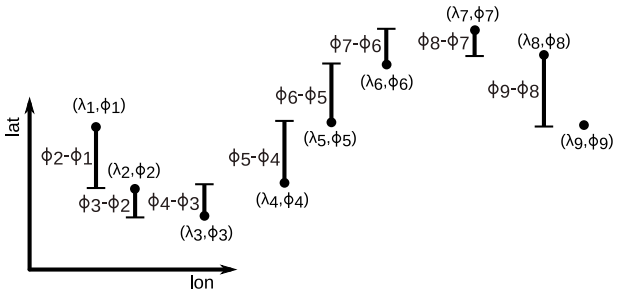

Figure 3. Schematic of a contour segment. The points of the contour are represented by dots and bars depict latitude differences between consecutive points of the contour segment. The waviness d corresponds to the sum of the lengths of the individual bars.

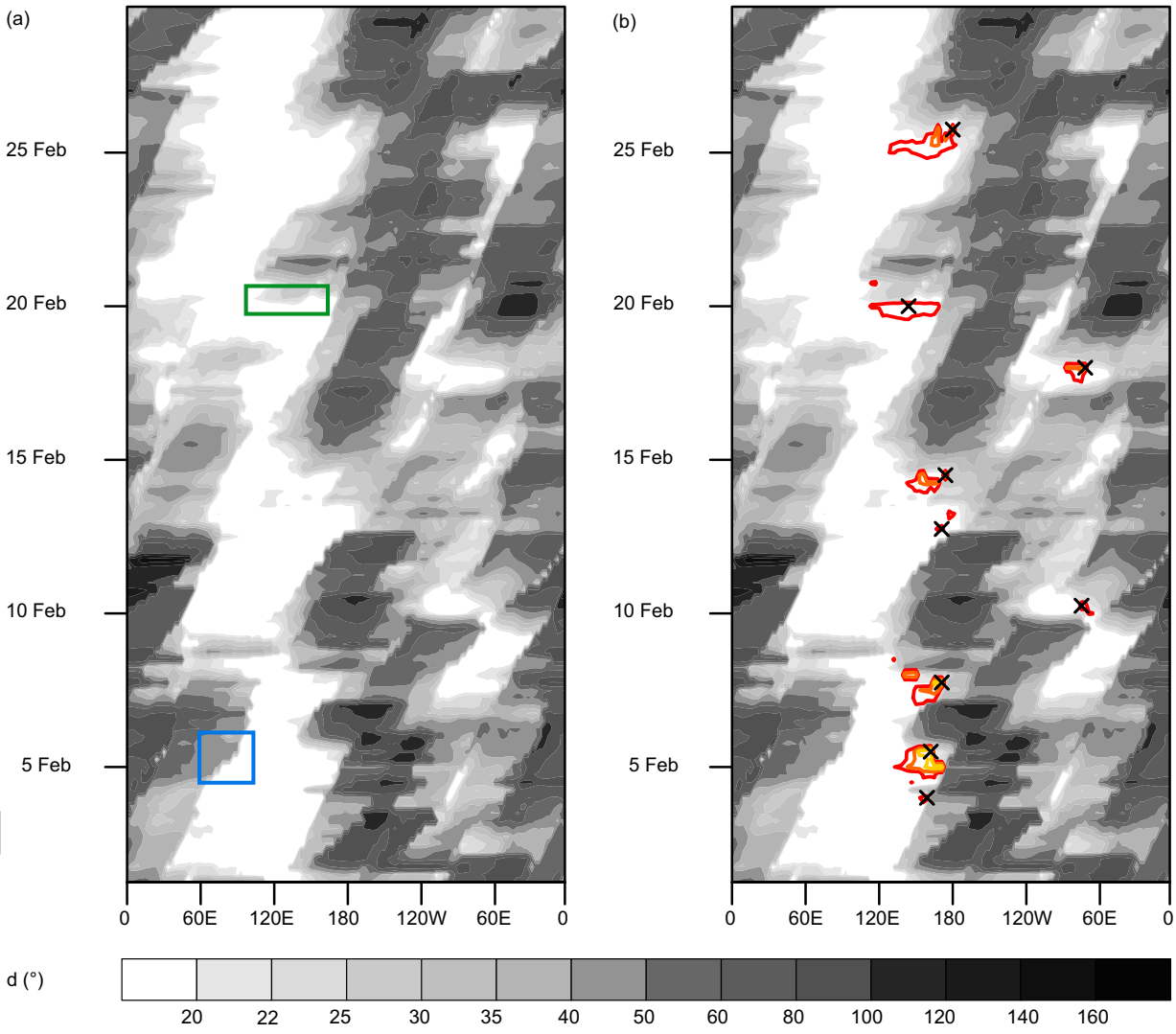

Figure 4. (a) d-Hovmöller diagram on 320 K in February 2000. The green box indicates segments and a time window with Rossby wave initiation characteristics, the blue box indicates a region where increasing d-values are due to an upstream wave propagating into a wave-free segment. (b) Same d-Hovmöller diagram as in a) but with contours of $g = 8$, 16 and 24 ° (red, orange and yellow), respectively. Black crosses indicate the identified RWIs.

a Hovmöller diagram. We refer to this diagram as d-Hovmöller diagram. Note that, in contrast to conventional Hovmöller diagrams, d-Hovmöller diagrams do not depict a latitudinally averaged quantity, as d is defined only the in longitude-time space on different isentropes.

Figure 4(a) shows the d-Hovmöller diagram on 320 K in February 2000. At longitude λ the d-value indicates d of the segment extending from longitude λ to $\lambda + 60\,^\circ$. The green box indicates segments and a time window where, qualitatively, Rossby wave initiation characteristics are met, i.e. where d is low in the beginning and rapidly increases at a location and time when d is small upstream. Segments in the blue box experience an increase in d over time but at the same time large d-values are recorded upstream,

Table 1. Important quantities used in the algorithm

Symbol	Value	Purpose/Definition
d_j^t		waviness in segment j at time t
g_j^t		growth of d in segment j at time t, i.e. $\frac{1}{5}\sum_{i=1}^{5} d_j^{t+i} - d_j^t$
u_j^t		$\max(d_{j-i}^t - d_j^t), i = 1...15$ for segment j at time t
d^*	$20\,^\circ$	separation of wavy and wave-free segments
u^*	$4\,^\circ$	identification of candidate segments with upstream wave
g^*	$8\,^\circ$	minimum g-value required for a RWI

pointing to the presence of an upstream wave. Thus, the increase in d is due to a wave propagating into these segments and does not represent a RWI.

RWI identification

RWIs are identified in individual segments, i.e. at specific points in the d-Hovmöller diagram, based on a four step approach described below. In this procedure, several parameters are introduced and have to be specified. Table 1 summarizes important quantities and the most important tuning parameters of the algorithm. The sensitivity of the algorithm output to changes in these parameters is further discussed in the Supporting Information. In order to identify RWIs in d-Hovmöller diagrams, the following four steps are carried out.

1. *Selection of wave-free segments j at time t by selecting segments with $d_j^t < d^*$ with $d^* = 20\,^\circ$.* These segments are from now on referred to as candidate segments.
2. *Identification of candidate segments, that show an increase of waviness with time.* In this step, for each candidate segment j at time t the quantity g_j^t is calculated. g_j^t measures the growth of d in segment j and it is equal to the mean d-value of the five successive time steps minus the d-value of the candidate segment at time t, i.e.

$$g_j^t = \frac{1}{5}\sum_{i=1}^{5} d_j^{t+i} - d_j^t. \tag{2}$$

   For segments with $d_j^t > d^*$, g_j^t is set to 0.
3. *Identification and elimination of candidate segments for which increasing d-values are due to an upstream wave propagating into the segment.* This separation is performed based on an upstream criterion that is explained in detail below. Candidate segments violating this criterion receive a g_j^t-value of zero.
4. *Identification of RWIs as local maxima in the field of g-values for which $g_j^t > g^*$ with $g^* = 8\,^\circ$.*

The threshold d^* was chosen by subjectively evaluating the identified events based on different thresholds. If choosing a very small value, many interesting events are missed due to sub-synoptic-scale undulations of the contour. Such small-scale undulations within an otherwise zonal segment substantially increase its d-value and hence hinder the identification of a RWI in this segment. If choosing a very large value, many cases are identified where pre-existing wave crests are amplified but no wave initiation occurs. Figure S1 (Supporting Information) illustrates two cases that guided us to set $d^* = 20\,^\circ$.

The time window used to calculate the g-values was chosen such that it covers the time typically needed for a wave-free contour segment to become clearly wavy. After analyzing numerous RWIs identified with various time window lengths we set this tuning parameter to 30 h (5 time steps). Note that enlarging or shortening this time window by one time step only marginally affects the number of identified RWIs and does not alter our main conclusions (see Supporting Information, Section 3).

The upstream criterion introduced in the third step evaluates whether the contour upstream of a candidate segment is sufficiently wave-free to exclude the presence of an upstream wave in a defined upstream range. The longitudinal extent of this range critically

depends on the maximum group velocity of Rossby wave packets as well as on the time window that is used to calculate the g-values. Several studies have determined the group velocity of Rossby wave packets (i.e. Hovmöller 1949; Chang and Yu 1999; Glatt and Wirth 2014) and found values of up to 30 ° longitude per day in the midlatitudes. Since the calculation of g-values is based on five time steps (30 h), we assume that wave packets located more than 45 ° upstream of a candidate segment have no influence on its d-value at the end of this time period. The extent of this range was therefore set to 45 °, which corresponds to 15 segments. In order to keep only candidate segments with no wave within this upstream range, the maximum difference between the d-values of the 15 segments upstream and the d-value of the candidate segment itself is calculated for each candidate segment. For a candidate segment j at time t we refer to this quantity as u_j^t and

$$u_j^t = \max(d_{j-i}^t - d_j^t), i = 1...15. \tag{3}$$

A large value of u_j^t implies the presence of a Rossby wave in the 15 segments upstream of the candidate segment, which could potentially propagate into the segment within the next five time steps. For each candidate segment j at time t with $u_j^t > u^*$ and $u^* = 4\,^\circ$ it is thus assumed that an upstream wave is present and the segment is eliminated by setting g_j^t to zero. The threshold $u^* = 4\,^\circ$ was chosen analogously to d^* by subjectively evaluating the identified RWIs using a range of different u^* values. In the Supporting Information (Figure S3) two cases are presented that guided us to choose this value for u^*. Note that with this upstream criterion the maximum allowed d-value within the upstream range depends on the d-value in the candidate segment itself. This is superior to a fixed threshold, as it guarantees that the upstream criterion is equally stringent for all candidate segments. If the upstream criterion was based on a fixed threshold, it would be less stringent for candidate segments with a very low d-value than for candidate segments with a d-value close to d^*.

The first three steps result in a set of g-values as a function of longitude and time ($g_j^t, j = 1...120, t = 1...T$) and large g-values indicate segments with initiation characteristics. In the fourth and final step, RWIs are identified as local maxima of g exceeding a threshold value $g^* = 8\,^\circ$. By setting g^* much larger than u^* we ensure that the increase in d in an initiation segment cannot solely result from small amplitude waves (not violating the upstream criterion) propagating into the initiation segment and, hence, an in situ initiation mechanism must be active. As for d^* and u^*, our choice of $g^* = 8\,^\circ$ is further discussed in the Supporting Information.

Example cases

We now turn back to the d-Hovmöller diagram for February 2000 (Figure 4) and apply the four step approach. Figure 4(b) shows the resulting g-contours of 8, 16 and 24 ° overlaid onto the d-Hovmöller diagram. Clearly, large g-values appear whenever d increases over time and no large d-values are recorded within a 45 ° range upstream at the respective time. A total of nine RWIs (indicated with black crosses) are identified in this month. Seven RWIs are located in the North Pacific region and two in the North Atlantic. The g-contours reveal that for some RWIs, multiple local maxima exceeding 8 ° exist (for example on 14 February at 135 °E). In such cases only the largest maximum in a 45 ° longitude and 18 h time window is identified as a RWI, to ensure that individual events are not identified more than once.

3. Results and discussion

Before discussing the climatology of RWIs we present three example RWIs identified by the algorithm. On the one hand, these example cases are meant to further portray the functioning of the algorithm. On the other hand they serve to illustrate the diversity of the dynamics leading to RWIs, as in each of the three cases a distinct initiation mechanism can be identified. Note however, that with these three example cases we do not aim at presenting a complete catalogue of initiation mechanisms.

3.1. *Case studies*

3.1.1. *Upper-tropospheric low-PV anomaly*

We start by discussing a RWI that occurred on 320 K at 1200 UTC 14 February 2004 in the contour segment starting at 174 °W. Figure 5 gives an overview of the synoptic situation and shows the geometry of the 2 PVU contour. Additionally, a d-Hovmöller diagram for 13-16 February 2004 on 320 K is presented in Figure 7(a). Twelve hours before the time of initiation (Figure 5(a)), a breaking wave is present within the initiation segment and the d-value of the segment is 62.31 °. The breaking wave is visible in Figure 7(a) as an area of high d-values moving eastward, located between approximately 180 °E and 120 °W at 0000 UTC 14 February. In the following 12 h the breaking wave moves out of the initiation segment and leaves the contour zonally aligned within the segment (Figure 5(b), Figure 7(a)). At the time of initiation the d-value is 19.14 ° and it steadily increases over the successive five time steps to reach a value of 35.56 ° at 1800 UTC 15 February, which results in a g-value of 12.63 °. Upstream of the initiation segment no synoptic-scale wave is present and thus none of the 15 segments upstream exhibit much larger d-values than the initiation segment itself (Figure 5(b), Figure 7(a)). With $u = 0.06$ ° the upstream criterion is not violated and a RWI is recorded at 1200 UTC 14 February (Figure 5(b,f)). Because of the criterion that only the strongest g-maximum is considered in a certain longitude-time window, the two g-peaks near 170 °E at 14 February in Figure 7(a) are not regarded as RWIs by our approach. This might appear as a caveat, but the same criterion prevents us from identifying spurious/too many RWIs in numerous other cases.

The PV evolution on 320 K (Figure 5(a-d)) reveals the formation of a ridge at approximately 140 °W. The ridge forms to the north of a tongue of moist air (at approximately 175 °W and 28 °N in Figure 5(e)) which is approaching the waveguide from the southwest (Figure 5(e-h)). At the time of initiation, this tongue is co-located with strong ascent and strong diabatic heating (Figure 5(f)). Concurrently, the SLP field (Figure 6) reveals the presence of a strong extratropical cyclone with its center at 180 °E and 55 °N and with a surface trough extending southward towards the tongue of moist air (155 °W and approximately 30 °N). The area of strong ascent is located at the southern fringe of this surface trough and co-located with an area of low IR values (Figure 6). The low IR values imply the presence of high reaching clouds of a convective system, possibly resulting from the interaction between the surface trough and the tongue of moist air. As this convective system moves north-eastward and intensifies (Figure 5(e-g)), negative PV values appear downstream of the convective system on 320 K (Figure 5(f,g)), indicating ongoing diabatic PV destruction at upper levels (Wernli and Davies 1997). This upper-level negative PV anomaly deforms the 2 PVU contour and leads to the increase in d that is identified by the algorithm.

In agreement with the findings of Rodwell *et al.* (2013) and Stensrud (2013), this case highlights the importance of diabatic processes in large convective systems to modulate upper-level waveguides. It illustrates the pathway from strong subtropical convection to a Rossby wave response on the extratropical jet. First, the convective system forms and intensifies. Then, an upper-level low-PV anomaly develops. Finally, a wave forms when the convective system and the associated low-PV anomaly approach the waveguide.

The interplay between diabatic processes and pre-existing waves on upper-level waveguides has been studied before (e.g. Massacand *et al.* 2001; Grams *et al.* 2011). The case presented here adds to these studies that PV destruction at upper levels due to strong diabatic processes can not only modify pre-existing waves, but is also able to initiate waves on an originally wave-free waveguide, provided it occurs close to the latter.

3.1.2. *Lower-stratospheric high-PV anomaly: Meso-scale high-PV anomaly*

The second case involves a meso-scale lower stratospheric high-PV anomaly (Cavallo and Hakim 2009; Kew *et al.* 2010) that impacts both waveguides over eastern Asia from the north (Figure 8.) Figure 7(b,c) indicates that at 0000 UTC 6 January 2007, a RWI is identified on the extratropical waveguide (320 K) at 126 °E and a second one 6 h later at 141 °E on the subtropical waveguide (340 K).

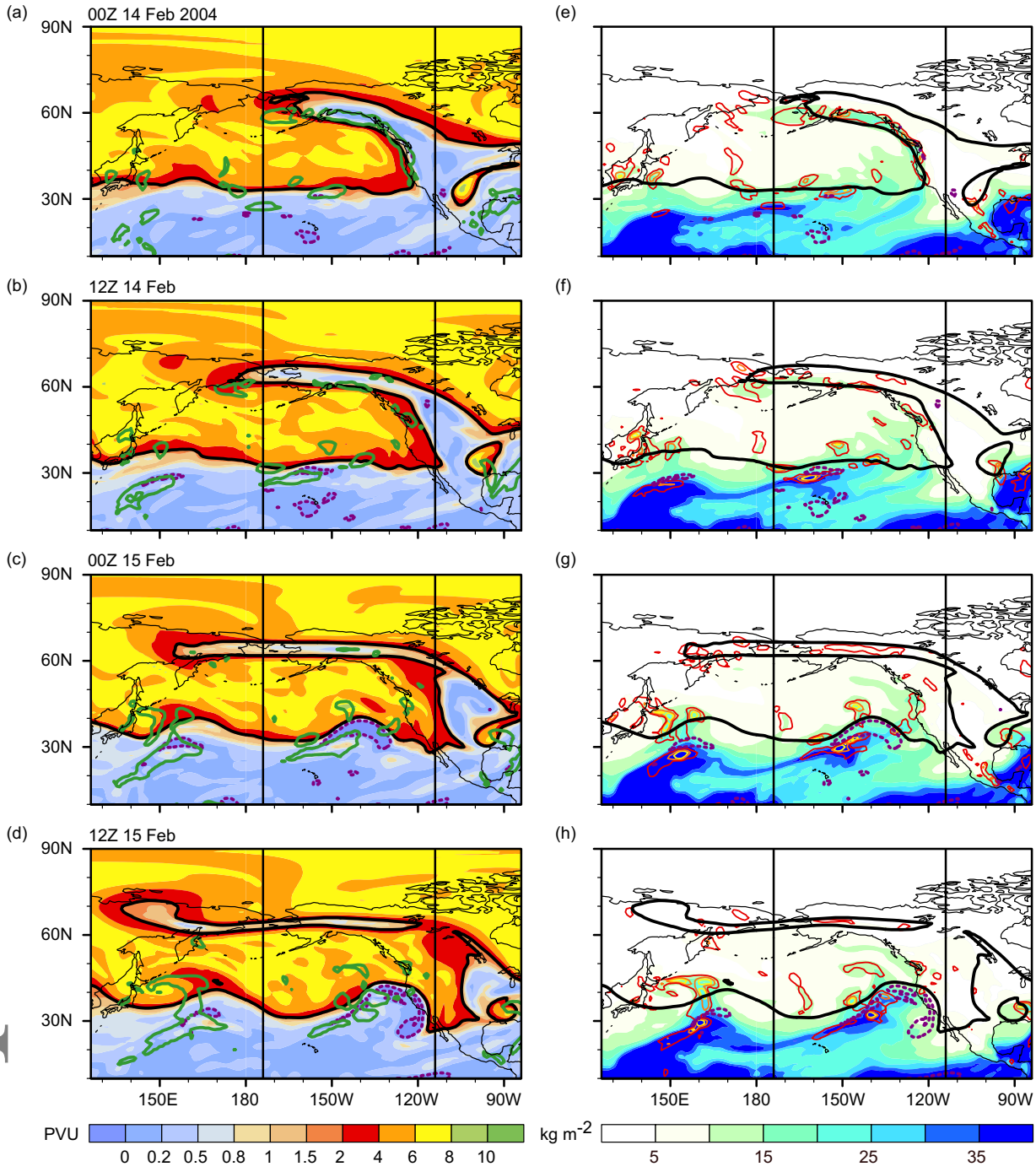

Figure 5. (a-d): PV on 320 K, vertical lines indicate the location of the initiation segment. Green contours indicate areas where vertically averaged (1000–300 hPa) diabatic heating due to condensation exceeds 1 K $(6\,h)^{-1}$. Black solid and purple stippled contours depict 2 and 0 PVU, respectively. (e-h): Vertically integrated (1000–300 hPa) specific humidity in kg m^{-2}, 2 and 0 PVU contours (as in panels (a-d)) and contours of vertical motion on 700 hPa of -10,-30 and -50 hPa h^{-1} (red, orange and yellow).

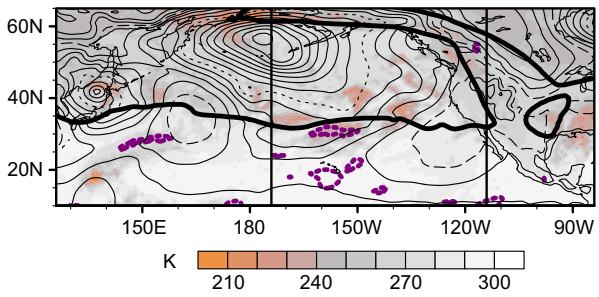

Figure 6. TOA brightness temperature near 11 microns (GridSat-B1) at 1200 UTC 14 February, 2 and 0 PVU contours (ERA-Interim) as in Figure 5(b,f) and SLP (ERA-Interim) with a contour spacing of 4 hPa 2004. Long-dashed and dashed SLP contours indicates 1020 hPa and 1000 hPa.

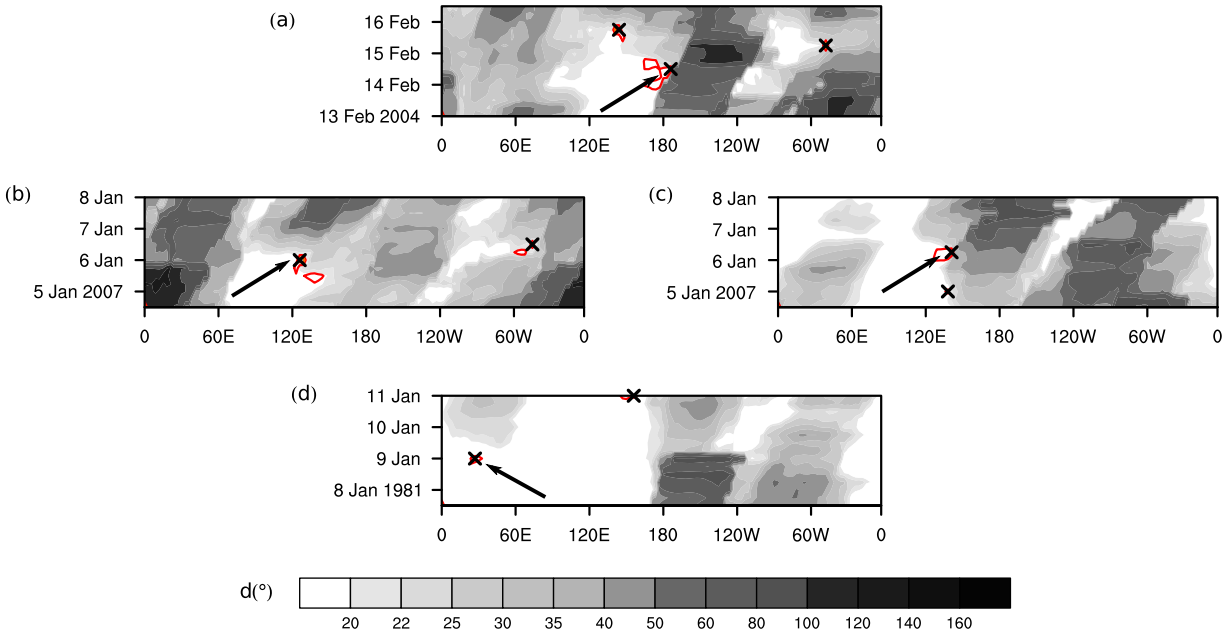

Figure 7. d-Hovmöller diagrams on 320 K (a,b) and 340 K (c,d) as in Figure 4 covering the times of initiation for the cases presented in subsections 3.1.1 (a), 3.1.2 (b,c) and 3.1.3 (d). Arrows indicate the RWI which is presented in the respective subsection. g-contours as in Figure 4.

The inspection of both 2 PVU contours reveals that at 0000 UTC 6 January, the two waveguides are vertically co-aligned (not shown). Therefore the initiation mechanism (to be discussed in the following paragraph) disturbs both waveguides simultaneously. Such co-occurring RWIs are further discussed in Section 3.2. In the following, this RWI is analyzed based on its evolution on 320 K, i.e. focusing on the extratropical waveguide.

Twelve hours prior to the time of initiation, at 1200 UTC 5 January 2007, the high-PV anomaly is visible north-west of Korea as a closed 6.5 PVU contour (Figure 8(a)). The wind arrows reveal the cyclonic flow field induced by this high-PV anomaly. At the time of initiation, i.e. 0000 UTC 6 January, the 2 PVU contour in the initiation segment is not perfectly wave-free, as the cyclonic flow field induced by the approaching high-PV anomaly has already started to affect the geometry of the 2 PVU contour in this segment (Figure 8(b)). Its d-value is 16.58 ° and the maximum d-value in the 15 segments upstream is 18.13 °, hence $u = 1.55$ °. Over the next 30 h a strong ridge forms and leads to a rapid increase in d (g=22.55 °), which the algorithm records as a RWI. The formation of this ridge is accompanied by strong diabatic heating (Figure 8(a-d)). The strong increase in d due to the ridge formation is also apparent in the corresponding d-Hovmöller diagram between 90 and 135 °E (Figure 7(b)). Additionally, the PV-trough at 80 °E in Figure 8(b) causes large d-values in segments starting around 45 °E, however, it does not propagate into the initiation segment during the 30 h after the time of initiation (as can also be seen from the 2 PVU contours in Figure 8(a-d)).

Figure 8(e-h) displays the concomitant evolution of SLP and potential temperature on 850 hPa. Twelve hours prior to the initiation, a baroclinic zone is located over the Sea of Japan and the high-PV anomaly lies above cold air over the continent. As the high-PV anomaly crosses the Sea of Japan, a strong surface cyclone with frontal systems develops rapidly ahead of the high-PV anomaly (Figure 8(g,h)).

The central element of this RWI is the meso-scale high-PV anomaly approaching the waveguide from the north. It does not only impact the geometry of the waveguide by means of barotropic vortex dynamics (i.e. via its far field effect), but also by means of baroclinic development. The small-amplitude undulation of the 2 PVU contour ahead of the high-PV anomaly at 0000 UTC 6 January (Figure 8(b)) conceivably results from the cyclonic wind field induced by the high-PV anomaly. At the same time, the SLP field shows only a weak pressure signal (minimum pressure 1007.2 hPa) ahead of the high-PV anomaly indicating little interaction between upper-level PV and lower-level temperature. However, as the high-PV anomaly crosses the baroclinic zone over the Sea of Japan, it starts

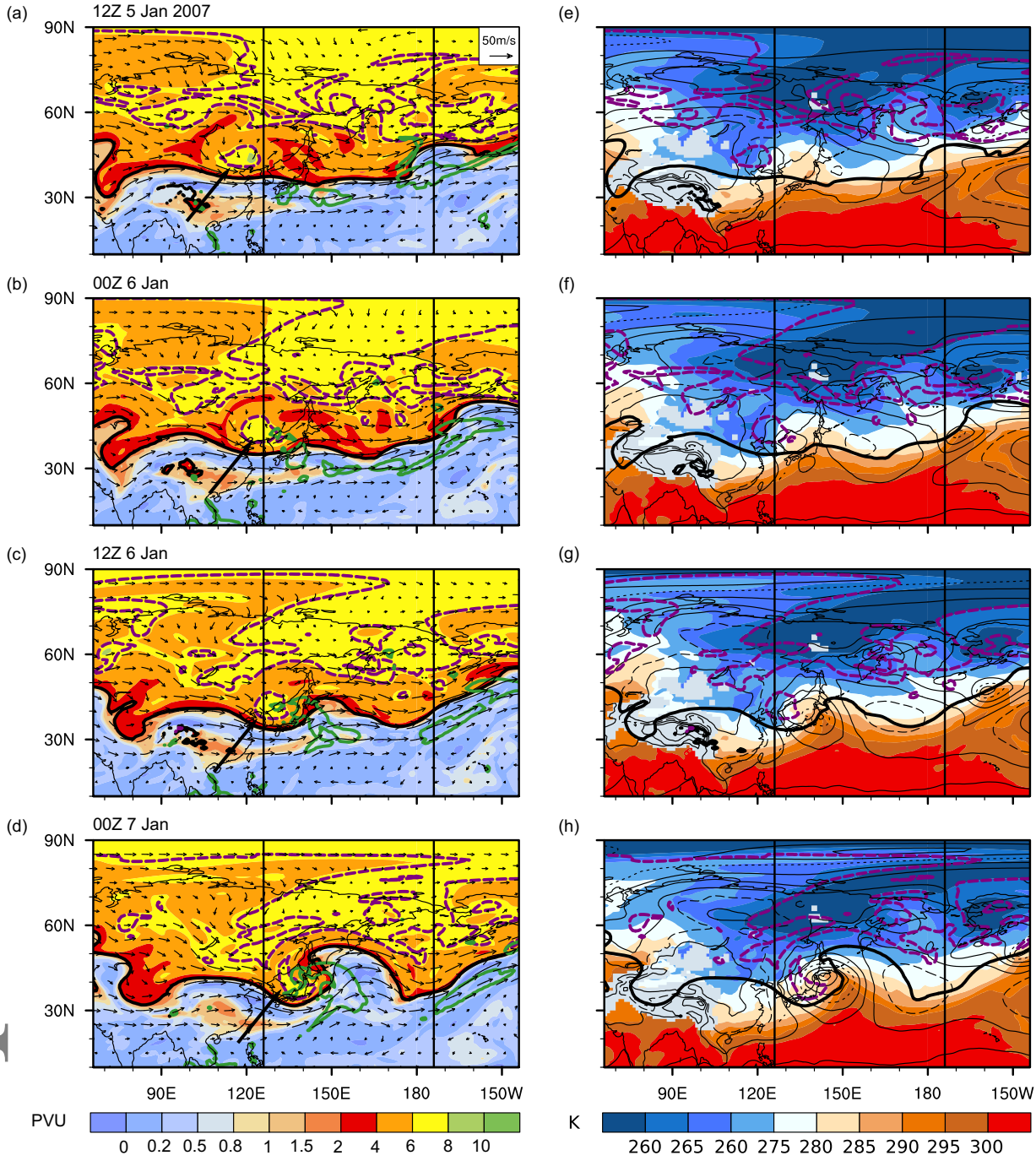

Figure 8. (a-d): PV and wind on 320 K. Green contours for condensational heating (K $(6h)^{-1}$) as in Figure 5. The 2 PVU contour (bold black) and the 6.5 PVU contour (dashed purple) are marked in each panel. The high-PV anomaly of interest is indicated with a black arrow and the initiation segment with vertical lines. (e-h): potential temperature on 850 hPa and SLP with 8 hPa contour intervals. Long-dashed and dashed SLP contours indicates 1028 hPa and 996 hPa.

to interact strongly with the surface baroclinicity and a strong cyclone develops. Within 24 h the minimum central SLP decreases to 965.4 hPa—a drop of almost 42 hPa within 24 h. Additionally, within the deepening cyclone strong condensational heating occurs, resulting in diabatic PV destruction at upper levels (Wernli and Davies 1997), which acts to further amplify the ridge at 150 °E. At 0000 UTC 7 January the amplifying wave shows many key features of a baroclinic wave with interacting, phase shifted waves in the upper-level PV field and the near-surface potential temperature field respectively. Baroclinic development certainly plays a key role in the rapid amplification of the forming wave. However, as baroclinic instability requires pre-existing waves at upper and lower levels (Heifetz *et al.* 2004), it acts as an amplification rather than initiation mechanism.

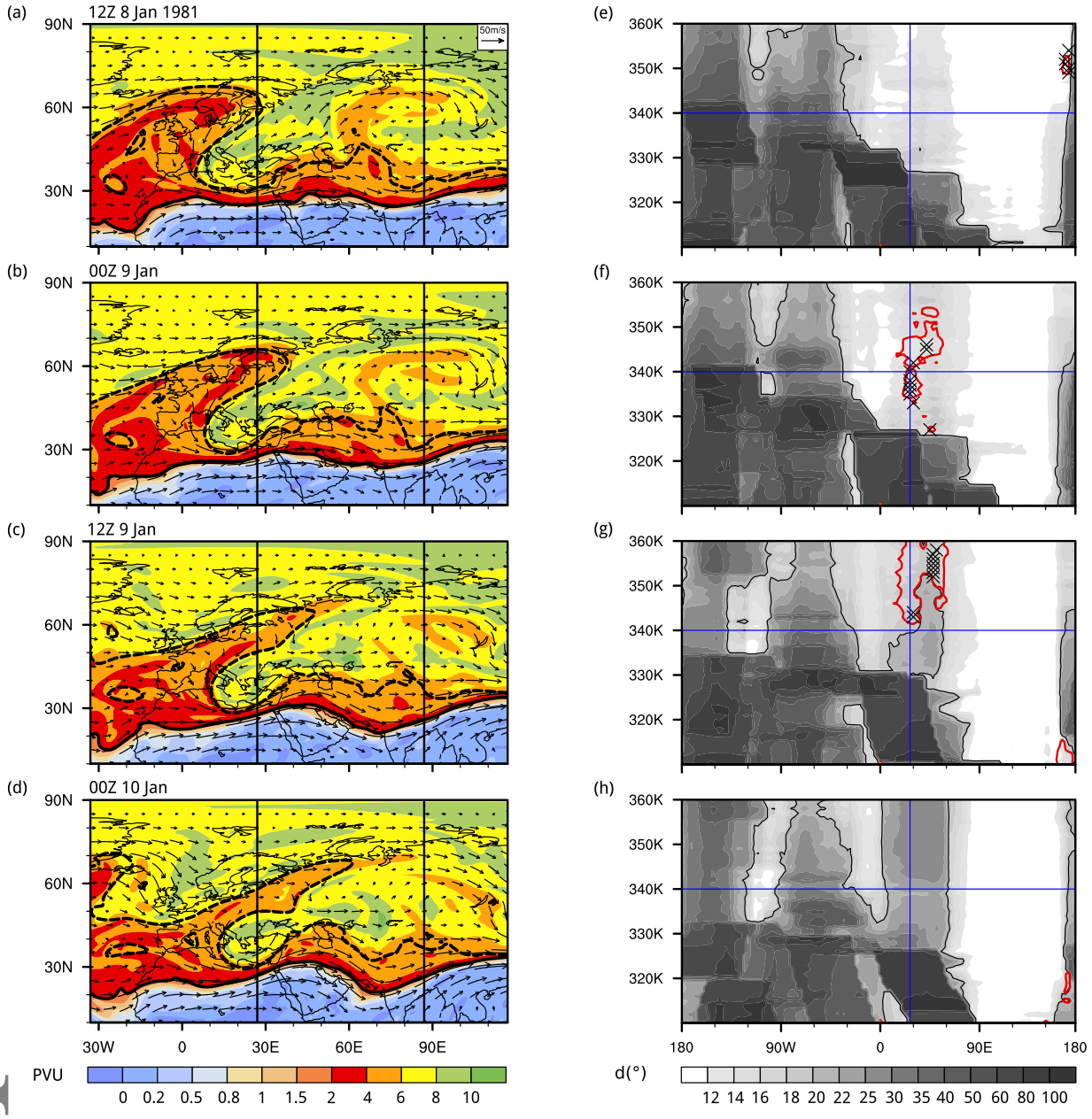

Figure 9. (a-d): PV (shading) and wind on 340 K. Black dashed contour indicates the 2 PVU contour on 320 K. Vertical lines indicate the initiation segment. (e-f): d as a function of longitude and potential temperature. The vertical blue line depicts the starting longitude of the initiation segment and the horizontal line marks the 340 K isentrope. Solid contour depicts $d = 20\,^{\circ}$. Red contour and black crosses depict $g = 8\,^{\circ}$ and identified RWIs on the respective level. Note that the gray scale in panels (e-f) is slightly different than for Figure 4 and 7.

3.1.3. Lower-stratospheric high-PV anomaly: Breaking wave

In this last case study, a RWI on the subtropical jet is presented, which is initiated by a breaking wave on the extratropical waveguide. The d-Hovmöller diagram on 340 K for 7–10 January 1981 (Figure 7(d)) shows a RWI identified at 0000 UTC 9 January 1981 in the segment starting at 27 °E. During 9 and 10 January d-values are slowly but steadily increasing for segments starting between 10 and 60 °E. At the time of initiation, the subtropical waveguide is free of large amplitude waves in almost the entire Eastern Hemisphere. Figure 9(a-d) shows the PV evolution and wind on 340 K for this RWI. At the time of initiation (Figure 9(b)), the 2 PVU contour on 340 K is not perfectly zonal within the initiation segment, however no clear wave is present. The d-value in the initiation segment is 12.73 ° and thereafter increases to 24.55 ° during the next 36 hours until 1200 UTC 10 January. The upstream criterion is not violated (u=0.74 °) and thus a RWI is identified with $g = 8.80\,^{\circ}$. Twelve hours prior to the initiation (Figure 9(a)), the 2 PVU contour on 340 K is already rather zonally aligned in the initiation segment and the 2 PVU contour on 320 K (black dashed contour) reveals the presence of an anticyclonically breaking wave on the extratropical jet. The high-PV part of the breaking wave approaches the relatively undisturbed

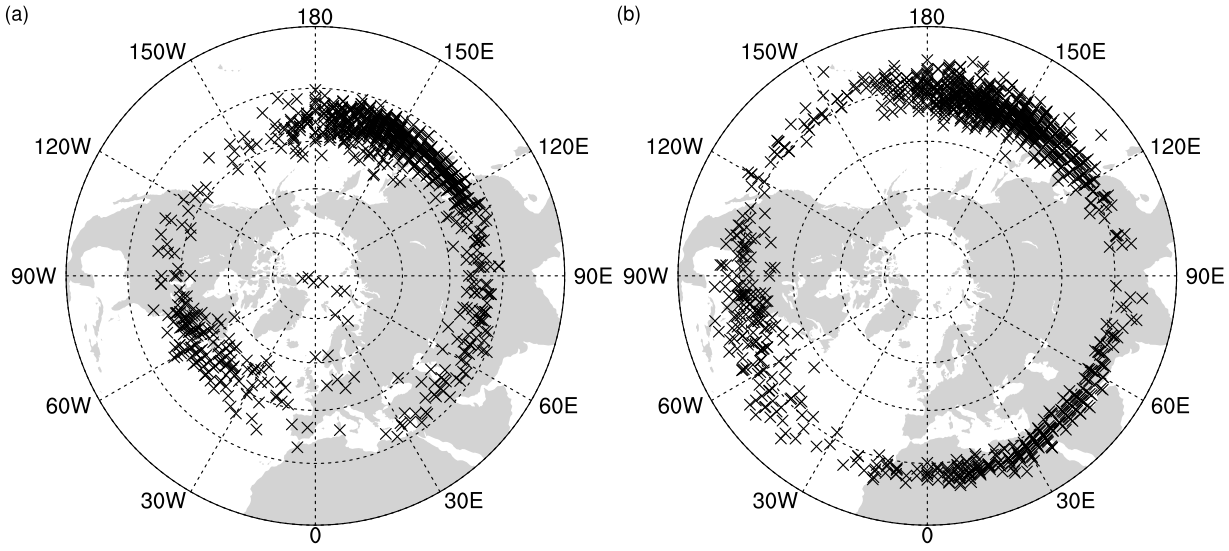

Figure 10. Climatology of RWIs in winters 1979/80-2013/14 on 320 K (a) and 340 K (b). Each cross indicates the longitude of the most upstream point of an initiation segment and its mean latitude.

subtropical waveguide (Figure 9(b)). The cyclonic flow field induced by the approaching high-PV anomaly deforms the 2 PVU contour on 340 K. As a consequence, a ridge and a downstream trough form in the initiation segment over the next 24 h (Figure 9(c,d)). Due to the cyclonic flow field, generally negative (positive) PV advection in the region of the forming ridge (trough) is found on 340 K when the ridge-trough couple amplifies, i.e., 0000 UTC 9 January and 1200 UTC 9 January (not shown).

Figure 9(e-h) displays the waviness measure d as a function of longitude and potential temperature for the same times as shown in panels a-d. The transfer of waviness from one waveguide to another is clearly visible. At the time of initiation (Figure 9(f)), the 2 PVU contours representing the extratropical waveguide (approximately 310-325 K) exhibit large d-values in segments starting between 0 and 60 °E as a result of the breaking wave. Above 327 K, the d-values are below 20 ° in these segments. However, over the next 24 h d-values start to increase on these levels as the ridge (at 45 °E) and the downstream trough (at 75 °E) form on the subtropical waveguide. At the longitude of the initiation, waviness is transferred equatorward and from lower to higher isentropes rather than downstream along the subtropical waveguide (Figure 9(g,h)). To further illustrate this argument, the four step approach described in Section 2.3 is applied to d-Hovmöller diagrams for isentropic levels between 310 and 360 K, separated by 1 K. Large g-values and RWIs identified on these levels are also shown in Figure 9(e-h). At 0000 UTC 9 January (Figure 9(f)) RWIs are identified on a number of isentropes close to 340 K. 12 h later, RWIs are recorded at higher isentropic levels and slightly further downstream, which is an additional hint for the transfer of waviness from lower to higher isentropes. Following Martius *et al.* (2010), we interpret this case as a RWI due to waveguide interaction and the lower-stratospheric high-PV anomaly associated with the breaking wave on the extratropical jet initiates the newly forming wave on the subtropical jet.

3.2. Climatology of RWIs

The algorithm is now applied to all winter seasons in 1979/80-2013/14. The location of all 884 RWIs on 320 K (representing RWIs on the extratropical waveguide) and 1159 RWIs on 340 K (on the subtropical waveguide) is shown in Figure 10. On both levels, the majority of the RWIs occur over the western Pacific. A secondary initiation region is located over North America and the North Atlantic. On 340 K a third initiation region is apparent, extending from the North African west coast across the Middle East (Figure 10(b)).

Over the Pacific, the initiation regions on the two levels partly overlap. This raises the question whether some RWIs are recorded on both levels simultaneously and are thus counted twice, similarly to the case presented in Section 3.1.2. Figure 11 displays longitude histograms for RWIs on 320 K and 340 K, as well as for RWIs recorded on 320 K, for which a RWI was recorded on 340 K in

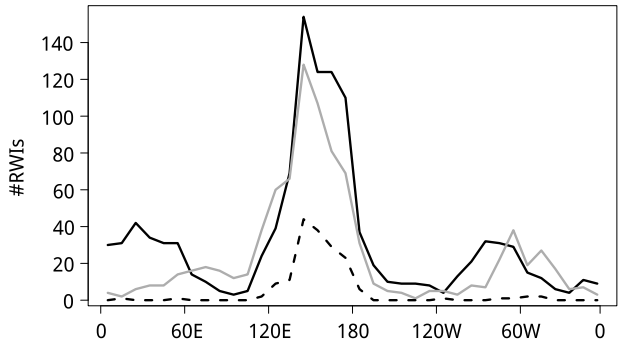

Figure 11. Longitudinal distribution of RWIs in bins of 10 ° longitude on 340 K (black), 320 K (grey) and RWIs on 320 K for which a RWI was recorded on 340 K in close longitudinal (15 °) and temporal (24 h) proximity (dashed) in DJF in 1979/80-2013/14.

close longitudinal (15 °) and temporal (24 h) proximity. For segments starting between 100 °E and 160 °W, i.e. segments located above the Pacific, quasi simultaneous identification of RWIs on both waveguides is rather frequent (25.2% of the RWIs on 320 K in these segments). In other initiation regions RWIs almost always occur exclusively on one waveguide only. This result highlights the importance of analysing the two waveguides separately, since in many regions of the Northern Hemisphere they are clearly distinct (albeit interacting) features of the upper-level flow. Note that the longitudinal distribution of these double counted events does not depend on the exact choice of maximum time and longitude differences used for their identification.

The climatological distribution of RWIs is in accordance with the findings of Souders *et al.* (2014a) and Glatt and Wirth (2014), who both applied feature-based techniques to identify Rossby wave packets in wave envelope data of upper-level meridional wind. Indeed, both studies found highest initiation frequencies over the Pacific, especially in winter, and a secondary maximum over North America. However, in contrast to our findings, neither of these studies found a large number of wave packet initiations over North Africa and the Middle East. We speculate that, for the study of Souders *et al.* (2014a), this is due to the use of 300 hPa meridional wind. This pressure level might be too low for detecting the initiation of wave packets propagating along the subtropical jet, which is typically located at higher levels (approximately 250-200 hPa). Glatt and Wirth (2014) used Hovmöller diagrams of wave envelope data on 250 hPa for which they performed a meridional averaging between 20 and 80 °N. As noted by Glatt *et al.* (2011), in double waveguide conditions as they frequently occur over Europe and North Africa, methods based on meridionally averaged data typically fail to capture the dynamics of the waveguides. For example the transfer of waviness from one waveguide to another (as described in Section 3.1.3) is difficult to detect in Hovmöller diagrams which depict meridionally averaged quantities. As suggested in Glatt *et al.* (2011), our approach circumnavigates this caveat by analysing the two waveguides separately.

4. Summary and conclusions

We developed a novel identification algorithm for the initiation of synoptic-scale Rossby waves on upper-level waveguides (RWIs). The algorithm identifies RWIs based on geometry changes of the 2 PVU contours on 320 K and 340 K, which serve as proxies for the position and geometry of the extratropical and subtropical waveguide respectively. The algorithm first determines the waviness of the 2 PVU contours for 60 ° long contour segments. Next, the algorithm searches for contour segments that are initially wave-free, i.e. have a low waviness, and whose waviness increases rapidly over time. Then the algorithm checks whether the waviness is large in a 45 ° sector upstream of these segments in order to exclude segments, where the increase in waviness results from upstream waves propagating into the segment. If this is not the case, the increase in waviness must result from an in situ process and thus a RWI is identified.

Arguably the most important caveat of our method is the fact that the number of identified RWIs depends on subjectively chosen tuning parameters. However, this is unavoidable, as the initiation of a synoptic-scale Rossby wave eludes a precise definition. Hence,

as also Glatt and Wirth (2014) noted, any "objective" identification algorithm for Rossby waves and their relevant properties must include subjectively chosen tuning parameters. Consequently, the absolute number of identified RWIs must be interpreted with care. Nevertheless, a large set of RWIs is a valuable source of insight on both the dynamical as well as climatological aspects of the formation of synoptic-scale Rossby waves.

We underlined this point by presenting in more detail three individual RWIs which all involve distinct wave initiation mechanisms. In the first case, a large convective system associated with strong diabatic heating leads to the formation of an upper-tropospheric low-PV anomaly. As this system approaches the extratropical jet, the low-PV anomaly interacts with the undisturbed waveguide and induces a wave on this waveguide. Hence the convective system acts as trigger of the forming wave. In the second case, a lower stratospheric meso-scale high-PV anomaly approaches the vertically co-aligned extratropical and subtropical waveguides over eastern Asia from the north and initiates a wave on both waveguides. The high-PV anomaly starts to interact with the surface baroclinicity, and a cyclone develops rapidly. The wave is then amplified by baroclinic development and diabatic PV reduction at upper levels further strengthens the ridge aloft. The third case illustrates a RWI on the subtropical jet over North Africa and the Middle East that involves waveguide interaction as described in Martius *et al.* (2010). An anticyclonically breaking wave on the extratropical jet acts as lower-stratospheric high-PV anomaly and approaches the undisturbed subtropical waveguide from the north. Through its far field effect, the PV anomaly induces a wave on the subtropical jet.

To provide a basis for further research on the earliest stage in the life cycle of synoptic-scale Rossby waves, we compiled a climatology of RWIs on the extratropical (320 K) and subtropical (340 K) waveguides in Northern Hemisphere winters. In accordance with the studies by Glatt and Wirth (2014) and Souders *et al.* (2014a), the west Pacific is identified as the main region where RWIs occur on both 320 K and 340 K. A second initiation region is found over North America and the North Atlantic on both levels. On 340 K only, North Africa and the Middle East stands out as a third initiation region, which has not been identified previously. Further, we found that RWIs evolving simultaneously on both waveguides are frequent only over the Pacific region. Elsewhere, RWIs almost exclusively occur on only one of the waveguides at a time.

The work presented in this paper offers a wide range of highly relevant follow-up research questions. For example, it provides a useful basis for studying climatological aspects of RWIs as well as the potential relationship between the variability of RWIs in the extratropics and the variability of tropical convection/heating. It is thus our hope that this study will serve as a first step towards a better understanding of the dynamical processes that govern the earliest stage in the life cycle of synoptic-scale Rossby waves.

Acknowledgement

We would like to thank two anonymous reviewers for their thoughtful reviews which helped to clarify the presentation of many aspects of our work. Further, we wish to thank MeteoSwiss and the ECMWF for providing access to the ERA-Interim data. This research was supported by the Swiss National Science Foundation (Grant number 200021_159905 / 1).

Supporting information

The following supporting information is available online: A detailed discussion of the selection procedure for the following tuning parameters: Segment length, time window which was used to calculate g, and the thresholds d^*, g^* and u^*. Where necessary, cases are presented that guided us to choose specific values for the tuning parameters.

Figure S1: PV evolution of two cases illustrating the choice of $d^* = 20\,^\circ$.

Figure S2: PV evolution of a false-positive case identified as RWI if g^* was chosen smaller than $8\,^\circ$.

Figure S3: PV evolution of two cases that were useful to determine u^* appropriately.

References

Archambault HM, Bosart LF, Keyser D, Cordeira JM. 2013. A climatological analysis of the extratropical flow response to recurving western North Pacific tropical cyclones. *Mon. Weather Rev.* **141**: 2325–2346, doi:10.1175/MWR-D-12-00257.1.

Cavallo SM, Hakim GJ. 2009. Potential vorticity diagnosis of a tropopause polar cyclone. *Mon. Weather Rev.* **137**: 1358–1371, doi:10.1175/2008MWR2670.1.

Chang EKM. 1993. Downstream development of baroclinic waves as inferred from regression analysis. *J. Atmos. Sci.* **50**: 2038–3053, doi:10.1175/1520-0469(1993)050⟨2038:DDOBWA⟩2.0.CO;2.

Chang EKM, Yu DB. 1999. Characteristics of wave packets in the upper troposphere. Part I: Northern Hemisphere winter. *J. Atmos. Sci.* **56**: 1708–1728, doi:10.1175/1520-0469(1999)056⟨1708:COWPIT⟩2.0.CO;2.

Coumou D, Petoukhov V, Rahmstorf S, Petri S, Schellnhuber HJ. 2014. Quasi-resonant circulation regimes and hemispheric synchronization of extreme weather in boreal summer. *P. Natl. Acad. Sci. USA* **111**: 12 331–12 336, doi:10.1073/pnas.1412797111.

Davies HC, Didone M. 2013. Diagnosis and dynamics of forecast error growth. *Mon. Weather Rev.* **141**: 2483–2501, doi:10.1175/MWR-D-12-00242.1.

Dee DP, Uppala SM, Simmons AJ, Berrisford P, Poli P, Kobayashi S, Andrae U, Balmaseda MA, Balsamo G, Bauer P, Bechtold P, Beljaars ACM, van de Berg L, Bidlot J, Bormann N, Delsol C, Dragani R, Fuentes M, Geer AJ, Haimberger L, Healy SB, Hersbach H, Hólm EV, Isaksen L, Kallberg P, Köhler M, Matricardi M, McNally AP, Monge-Sanz BM, Morcrette JJ, Park BK, Peubey C, de Rosnay P, Tavolato C, Thépaut JN, Vitart F. 2011. The ERA-Interim reanalysis: configuration and performance of the data assimilation system. *Q. J. Roy. Meteor. Soc.* **137**(656): 553–597, doi:10.1002/qj.828.

Glatt I, Dörnbrack A, Jones S, Keller J, Martius O, Müller A, Peters DHW, Wirth V. 2011. Utility of Hovmöller diagrams to diagnose Rossby wave trains. *Tellus* **63A**: 991–1006, doi:10.1111/j.1600-0870.2011.00541.x.

Glatt I, Wirth V. 2014. Identifying Rossby wave trains and quantifying their properties. *Q. J. Roy. Meteor. Soc.* **140**(679): 384–396, doi:10.1002/qj.2139.

Grams CM, Wernli H, Boettcher M, Campa J, Corsmeier U, Jones SC, Keller JH, Lenz CJ, Wiegand L. 2011. The key role of diabatic processes in modifying the upper-tropospheric wave guide: a North Atlantic case-study. *Q. J. Roy. Meteor. Soc.* **137**: 2174–2193, doi:10.1002/qj.891.

Hakim GJ. 2003. Developing wave packets in the North Pacific storm track. *Mon. Weather Rev.* **131**: 2824–2837, doi:10.1175/1520-0493(2003)131⟨2824:DWPITN⟩2.0.CO;2.

Hakim GJ. 2005. Vertical structure of midlatitude analysis and forecast errors. *Mon. Weather Rev.* **133**(3): 567–578, doi:10.1175/MWR-2882.1.

Heifetz E, Bishop CH, Hoskins BJ, Methven J. 2004. Counter-propagating Rossby-wave perspective on baroclinic instability. I: Mathematical basis. *Q. J. Roy. Meteor. Soc.* **130**: 211–231, doi:10.1256/qj.02.184.

Hoskins BJ, Ambrizzi T. 1993. Rossby wave propagation on a realistic longitudinally varying flow. *J. Atmos. Sci.* **50**: 1661–1671, doi:10.1175/1520-0469(1993)050⟨1661:RWPOAR⟩2.0.CO;2.

Hoskins BJ, Karoly DJ. 1981. The steady linear response of a spherical atmosphere to thermal and orographic forcing. *J. Atmos. Sci.* **38**(6): 1179–1196, doi:10.1175/1520-0469(1981)038⟨1179:TSLROA⟩2.0.CO;2.

Hoskins BJ, McIntyre ME, Robertson AW. 1985. On the use and significance of isentropic potential vorticity maps. *Q. J. Roy. Meteor. Soc.* **111**: 877–946, doi:10.1002/qj.49711147002.

Hoskins BJ, Woollings T. 2015. Persistent extratropical regimes and climate extremes. *Current Climate Change Reports* **1**(3): 115–124, doi:10.1007/s40641-015-0020-8.

Hovmöller E. 1949. The trough-and-ridge diagram. *Tellus* **1**: 62–66, doi:10.1111/j.2153-3490.1949.tb01260.x.

Jones SC, Harr PA, Abraham J, Bosart LF, Bowyer PJ, Evans JL, Hanley DE, Hanstrum BN, Hart RE, Lalaurette F, Sincair MR, Simth KR, Thorncroft C. 2003. The extratropical transition of tropical cyclones: Forecast challenges, current understanding, and future directions. *Weather Forecast.* **18**: 1052–1092, doi:10.1175/1520-0434(2003)018⟨1052:TETOTC⟩2.0.CO;2.

Kew SF, Sprenger M, Davies HC. 2010. Potential vorticity anomalies of the lowermost stratosphere: A 10-yr winter climatology. *Mon. Weather Rev.* **138**: 1234–1249, doi:10.1175/2009MWR3193.1.

Knapp KR, Ansari S, Bain CL, Bourassa MA, Dickinson MJ, Funk C, Helms CN, Hennon CC, Holmes CD, Huffman GJ, Kossin JP, Lee HT, Loew A, Magnusdottir G. 2011. Globally gridded satellite observations for climate studies. *Bull. Amer. Meteorol. Soc.* **92**: 893–907, doi:10.1175/2011BAMS3039.1.

Koch P, Wernli H, Davies HC. 2006. An event-based jet-stream climatology and typology. *Int. J. Climatol.* **26**: 283–301, doi:10.1002/joc.1255.

Langland RH, Shapiro MA, Gelaro R. 2002. Initial condition sensitivity and error growth in forecasts of the 25 January 2000 East Coast snowstorm. *Mon. Weather Rev.* **130**: 957–974, doi:10.1175/1520-0493(2002)130⟨0957:ICSAEG⟩2.0.CO;2.

Lee S, Held IM. 1993. Baroclinic wave packets in models and observations. *J. Atmos. Sci.* **50**: 1413–1428, doi:10.1175/1520-0469(1993)050⟨1413:BWPIMA⟩2.0.CO;2.

Madonna E, Wernli H, Joos H, Martius O. 2014. Warm conveyor belts in the ERA-Interim Dataset (1979-2010). Part I: Climatology and potential vorticity evolution. *J. Climate* **27**: 3–26, doi:10.1175/JCLI-D-12-00720.1.

Martius O, Schwierz C, Davies HC. 2008a. Far-upstream precursors of heavy precipitation events on the Alpine south side. *Q. J. Roy. Meteor. Soc.* **134**: 417–428, doi:10.1002/qj.229.

Martius O, Schwierz C, Davies HC. 2010. Tropopause-level waveguides. *J. Atmos. Sci.* **67**: 866–879, doi:10.1175/2009JAS2995.1.

Martius O, Schwierz C, Sprenger M. 2008b. Dynamical tropopause variability and potential vorticity streamers in the Northern Hemisphere a climatological analysis. *Adv. Atmos. Sci.* **25**(3): 367–380, doi:10.1007/s00376-008-0367-z.

Massacand AC, Wernli H, Davies HC. 2001. Influence of upstream diabatic heating upon an Alpine event of heavy precipitation. *Mon. Weather Rev.* **129**: 2822–2828, doi:10.1175/1520-0493(2001)129⟨2822:IOUDHU⟩2.0.CO;2.

Palmer T. 2014. Record-breaking winters and global climate change. *Science* **344**: 803–804, doi:10.1126/science.1255147.

Pyle M, Keyser D, Bosart LF. 2004. A diagnostic study of jet streaks: Kinematic signatures and relationship to coherent tropopause disturbances. *Mon. Weather Rev.* **132**: 297–319, doi:10.1175/1520-0493(2004)132⟨0297:ADSOJS⟩2.0.CO;2.

Riemer M, Jones SC. 2014. Interaction of a tropical cyclone with a high-amplitude, midlatitude wave pattern: Waviness analysis, trough deformation and track bifurcation. *Q. J. Roy. Meteor. Soc.* **140**: 1362–1376, doi:10.1002/qj.2221.

Riemer M, Jones SC, Davis CA. 2008. The impact of extratropical transition on the downstream flow: An idealized modelling study with a straight jet. *Q. J. Roy. Meteor. Soc.* **134**: 69–91, doi:10.1002/qj.189.

Rodwell MJ, Magnusson L, Bauer P, Bechtold P, Bonavita M, Cardinali C, Diamantakis M, Earnshaw P, Garcia-Mendez A, Isaksen L, Källén E, Klocke D, Lopez P, McNally T, Persson A, Prates F, Wedi N. 2013. Characteristics of occasional poor medium-range weather forecasts for Europe. *Bull. Amer. Meteorol. Soc.* **94**: 1393–1405, doi:10.1175/BAMS-D-12-00099.1.

Schwierz C, Dirren S, Davies HC. 2004. Forced waves on a zonally aligned jet stream. *J. Atmos. Sci.* **61**: 73–87, doi:10.1175/1520-0469(2004)061⟨0073:FWOAZA⟩2.0.CO;2.

Screen JA, Simmonds I. 2014. Amplified mid-latitude planetary waves favour particular regional weather extremes. *Nat. Clim. Change* doi:10.1038/nclimate2271.

Souders MB, Colle BA, Chang EKM. 2014a. The climatology and characteristics of Rossby wave packets using a feature-based tracking technique. *Mon. Weather Rev.* **142**: 3528–3548, doi:10.1175/MWR-D-13-00371.1.

Souders MB, Colle BA, Chang EKM. 2014b. A description and evaluation of an automated approach for feature-based tracking of Rossby wave packets. *Mon. Weather Rev.* **142**: 3505–3527, doi:10.1175/MWR-D-13-00317.1.

Stensrud DJ. 2013. Upscale effects of deep convection during the North American monsoon. *J. Atmos. Sci.* **70**(9): 2681–2695, doi:10.1175/JAS-D-13-063.1.

Thorncroft CD, Hoskins BJ, McIntyre ME. 1993. Two paradigms of baroclinic-wave life-cycle behaviour. *Q. J. Roy. Meteor. Soc.* **119**: 17–55, doi:10.1002/qj.49711950903.

Wernli H, Davies HC. 1997. A Lagrangian-based analysis of extratropical cyclones. I: The method and some applications. *Q. J. Roy. Meteor. Soc.* **123**: 467–489, doi:10.1002/qj.49712353811.

Wernli H, Sprenger M. 2007. Identification and ERA-15 climatology of potential vorticity streamers and cutoffs near the extratropical tropopause. *J. Atmos. Sci.* **64**: 1569–1586, doi:10.1175/JAS3912.1.

Wirth V, Eichhorn J. 2014. Long-lived Rossby wave trains as precursors to strong winter cyclones over Europe. *Q. J. Roy. Meteor. Soc.* **140**: 729–737, doi:10.1002/qj.2191.